Effect of strain rate on the compressive mechanical behavior of a continuous alumina fiber reinforced ZE41A magnesium alloy based composite

M. Güden [a,b,*], O. Akil [a], A. Tasdemirci [a], M. Çiftçioglu [b], I.W. Hall [c]

[a] *Mechanical Engineering Department, İzmir Institute of Technology, İzmir, Turkey*
[b] *Materials Science and Engineering Program, İzmir Institute of Technology, İzmir, Turkey*
[c] *Mechanical Engineering Department, University of Delaware, Newark, DE, USA*

Abstract

The compressive mechanical response of an FP[TM] continuous fiber (35 vol.%) Mg composite has been determined in the transverse and longitudinal directions at quasi-static and high strain rates. It was found that the composite in the transverse direction exhibited strain rate sensitivity of the flow stress and maximum stress within the studied strain-rate range of 1.3×10^{-4} to $1550\,s^{-1}$. The failure strain in this direction, however, decreased with increasing strain rate. Microscopic observations on the failed samples have shown that the composite failed by shear banding along the diagonal axis, 45° to the loading axis. Twinning was observed in the deformed cross-sections of the samples particularly in and near the shear band region. The strain rate sensitivity of the fracture stress of the composite in transverse direction is attributed to the matrix strain rate sensitivity. In the longitudinal direction, the composite failed by kink formation at quasi-static strain rates, while kinking and splitting were observed at the high strain rates. The maximum stress in the longitudinal direction was, however, found to be strain rate insensitive within the strain rate regime of 1.3×10^{-4} to $500\,s^{-1}$. In this direction, similar to transverse direction, twinning was observed in the highly deformed kink region. Several different reasons are proposed for the strain rate insensitive compressive strength in this direction.
© 2006 Elsevier B.V. All rights reserved.

Keywords: Magnesium; Composite; Compression; High strain rate

1. Introduction

Compared to their monolithic alloy counterparts, metal matrix composites (MMCs) usually provide higher strength and modulus, enhanced high temperature strength and wear resistance. Despite the high manufacturing costs, their outstanding thermo-mechanical properties make MMCs suitable materials for aerospace, defense and automobile industries where improved material performance may outweigh the cost penalty. Dynamic loading response is an important design parameter, which is critical in severe applications where impact loading occurs. Under impact conditions, the strain rate in the composite may locally reach strain rates in excess of $1000\,s^{-1}$. Therefore, high strain-rate mechanical response of MMCs is important in present and future applications in these industries.

Previous studies on high strain rate deformation behavior of MMCs mostly concentrated on particulate, short fiber and whisker reinforced MMCs [1–7], groups of MMCs having wider application fields. Few studies have been conducted on the high strain-rate response of continuous fiber reinforced MMCs and these were mainly on Al matrix composites [8–11]. Being the lightest common structural metal, Mg can potentially provide a high strength to weight ratio which is important in applications where weight saving is an important design criterion. Despite the many experimental investigations conducted to understand the deformation behavior and mechanical properties of magnesium metal matrix composites and unreinforced alloys at quasi-static strain rates, the mechanical properties of Mg based MMCs and unreinforced alloys at increasing strain rates have not been investigated as much.

Klimanek and Pötzsch [12] investigated the microstructural evolution of pure magnesium under compression at different strain rates between 10^{-3} and $500\,s^{-1}$ at room temperature and 150 °C. Flow stress increased with decreasing temperature and

* Corresponding author. Tel.: +90 232 7506595; fax: +90 232 7506505.
  E-mail address: mustafaguden@iyte.edu.tr (M. Güden).

with increasing strain rate, proving a strain rate sensitive flow stress behavior. The mean twin size was shown to decrease only slightly with increasing strain. The decrease in the twin volume fraction between 5 and 10% strains was explained by the multiple twinning, which reduced the size of the twins, making them invisible under an optical microscope. Mukai et al. [13] investigated the effect of grain refinement on the tensile ductility of pure Mg and a ZK60 Mg alloy under dynamic loading. It was shown that the yield strength of pure magnesium and ZK60 alloy increased with decreasing grain size at high strain rates ($1.8 \times 10^3 \, \text{s}^{-1}$), similar to the quasi-static strain rate behavior. The increase in yield strength at high strain rate as compared with quasi-static strain rate was found to be higher in the alloy than pure magnesium. Watanabe et al. [14] investigated the high strain rate superplasticity of ZK61 magnesium alloys. At strain rates below $1 \times 10^{-2} \, \text{s}^{-1}$ ZK61 alloy exhibited relatively low strain hardening and the flow stress was shown to increase with increasing strain rate. Takuda et al. [15] investigated the effect of strain rate on the deformation behavior of an MgLiZn alloy at $0°$, $45°$, and $90°$ to the rolling direction. It was shown that although increasing strain rate increased the flow stress, it decreased the ductility. Mukai et al. [16] investigated the effect of equal channel angular extrusion on the failure strain of AZ31 Mg alloy at quasi-static ($10^{-3} \, \text{s}^{-1}$) and high strain ($10^3 \, \text{s}^{-1}$) rates and showed that equal channel angular extrusion more than doubled the dynamic tensile failure strain as compared with direct extrusion. Ishikawa et al. [17] examined the high strain rate compression behavior of a solution treated AZ91 Mg alloy at elevated temperatures. The flow stress was shown to increase with increasing strain rate from 10^{-3} to $10^3 \, \text{s}^{-1}$. Essa et al. [18,19] investigated the damage and fracture mecha-

nisms of 12%, 10 μm size SiC_p reinforced Mg–5% Zn–1% Mn magnesium alloy at quasi-static and high strain rates using a tensional Split Hopkinson Pressure Bar (SHPB) set-up. It was found that dynamically tested composite and unreinforced alloy showed higher flow stresses than those of the quasi-statically tested counterparts. In dynamic tests at room temperature, the percentage of particles that fractured was higher than that which underwent particle/matrix decohesion while in quasi-static test at room temperature the percentages of broken and decohered particles were similar.

The main objective of this experimental study is to determine compressive mechanical properties of a long fiber reinforced Mg MMC as function of strain rate, which has not been investigated yet. The effect of strain rate on the important mechanical properties such as flow stress and failure stress and strain was determined. This study provides considerable new information on the compression properties of Mg matrix long fiber MMCs over a wide strain-rate range.

2. Experimental

The unidirectional continuous FP$^{\text{TM}}$ fiber 99% α-Al_2O_3 reinforced ZE41A Mg MMC plate was produced by E.I. Dupont Co. using a molten metal vacuum infiltration technique. In this technique, FP$^{\text{TM}}$ tapes were laid up with a fugitive binder in the desired orientation and fiber volume fraction to form a fiber preform which was then inserted into a steel casting mold. The fugitive binder was burned away and the mold was infiltrated with molten metal. The composite material studied was manufactured in the form of 12.8 mm thick plate and contained 35 vol.% fiber, determined microscopically using an image ana-
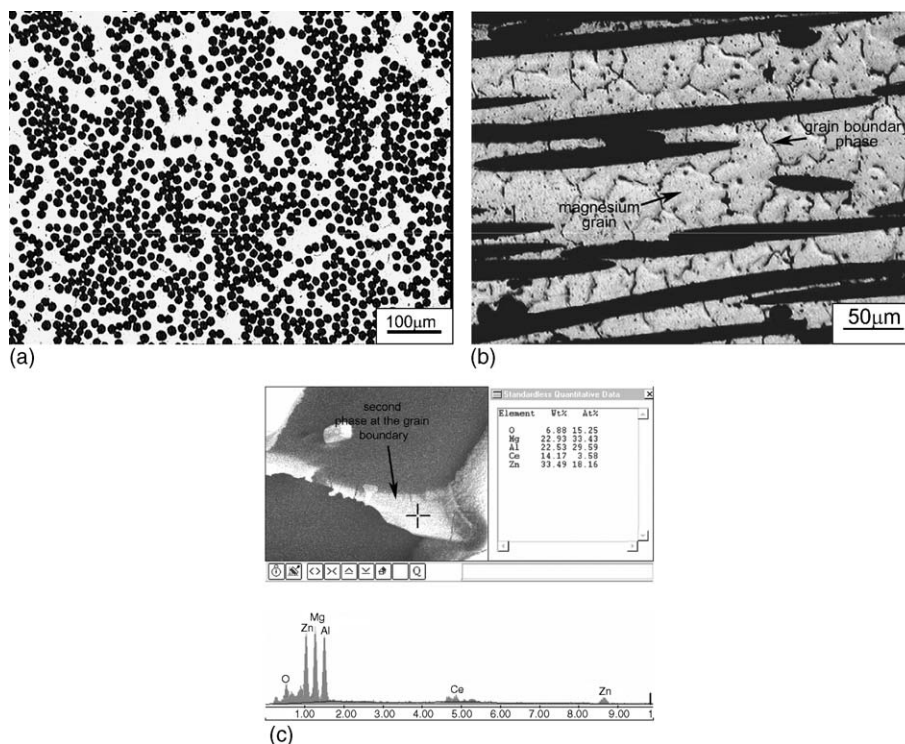

Fig. 1. The etched microstructure of the composite in the (a) transverse and (b) longitudinal directions and (c) EDX analysis of the grain boundary phase.

lyzer. The matrix alloy contained 4.2% Zn, 0.7% Zr and 1.2% Ce. Typical microstructures of the transverse and longitudinal sections of the MMC are shown in Fig. 1(a) and (b) and exhibit 100 μm size α-Mg grains. The grains are decorated with an Mg–Zn–Al–Ce quaternary phase determined by energy dispersive X-ray (EDX) analysis as depicted in Fig. 1(c). The average fiber diameter was 20 μm.

Quasi-static and dynamic compression tests were conducted on cylindrical core drilled specimens, 6.7 mm in diameter and 12.8 mm in length. Samples were tested in transverse and longitudinal directions, i.e. normal and parallel to the fiber axis. Quasi-static tests were conducted using a displacement controlled Shimadzu AG-I universal tension-compression test machine at cross-head speeds of 0.1, 3.2 and 100 mm min^{-1} corresponding to the strain rates of 1.3×10^{-4}, 4.16×10^{-3} and 1.3×10^{-1} s^{-1}, respectively. The displacement values of the compression test specimens were further corrected by subtracting the machine displacement (calculated from the measured machine compliance value) from the total displacement (machine + specimen). High strain rate tests were conducted using a compression SHPB, comprising three 19 mm diameter Inconel-718 bars: a striker bar (724 mm in length), an incident bar (3660 mm in length) and a transmitter bar (1830 mm in length). The striker bar produces a constant amplitude elastic compressive wave in the incident bar. The wave propagates down the bar to the bar/specimen interface where it is partly reflected back into the incident bar as a tensile pulse and partly transmitted to the transmitter bar as a compressive pulse. Strain gages on the incident and transmitter bars record the passage of the waves and these data are the input used for generating stress/strain curves. The characteristic time window for passage of the wave is ~290 μs and repeated loading of the specimen in between the bars is prevented by use of a transmitter bar that is half the length of the incident bar. Further details of SHPB testing may be found in Ref. [20]. The strain rate ($\dot{\varepsilon}$), strain (ε) and stress (σ) in the specimen are given by [20]:

$$\dot{\varepsilon}(t) = -\frac{2C_b}{L_s} \varepsilon_r(t) \tag{1}$$

$$\varepsilon(t) = -\frac{2C_b}{L_s} \int_0^t \varepsilon_r(t) \tag{2}$$

$$\sigma(t) = \frac{E_b A_b}{A_s} \varepsilon_t(t) \tag{3}$$

where C_b is the elastic wave velocity in the bar, L_s the sample length and A_s and A_b are the sample and bar cross-sectional areas, respectively. ε_r and ε_t are the reflected and transmitted strains measured from strain gages on the bar, respectively. For a specific test, the instantaneous strain rate varied during deformation from zero to final or failure strain, and therefore an average strain rate was calculated as

$$\dot{\varepsilon}_{avg} = \frac{1}{\varepsilon_f} \int_0^{\varepsilon_f} \dot{\varepsilon} \, d\varepsilon \tag{4}$$

where ε_f is the maximum or failure strain. The maximum temperature increase arising from the almost adiabatic conditions

of the testing procedure is in the range of 5–10 °C and does not influence the reported results.

Microscopic analyses were performed on the tested composite samples using optical microscopy and a Philips XL30-SFEG scanning electron microscope (SEM) with an EDX analyzer. Polished sample surfaces were etched with Kroll's reagent (3 cm^3 of HF and 6 cm^3 of HNO$_3$ in 100 ml of H$_2$O).

3. Results

3.1. Transverse direction

An example of SHPB strain reading of the specimen tested in the transverse direction and the corresponding stress and strain rate variation with strain are shown in Fig. 2(a) and (b), respectively. Since the strain rate varies with strain, an average strain rate is calculated until the failure strain as shown in Fig. 2(b). Typical quasi-static and high strain rate compression engineering stress–strain curves of the composite in the transverse direction are presented in Fig. 3. The initial elastic region of each curve is followed by a region of inelastic deformation until a maximum stress is reached, after which the sample fails by shear at 45° to the loading axis. The maximum stress and
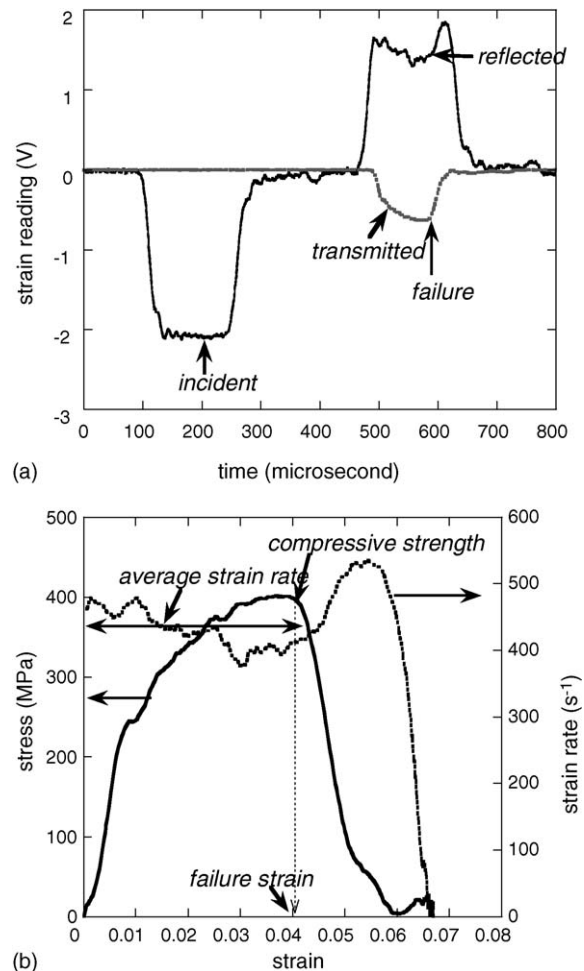
(a)

(b)

Fig. 2. Typical SHPB test results of the composite tested in the transverse direction (a) strain reading vs. time and (b) stress and strain rate vs. strain.
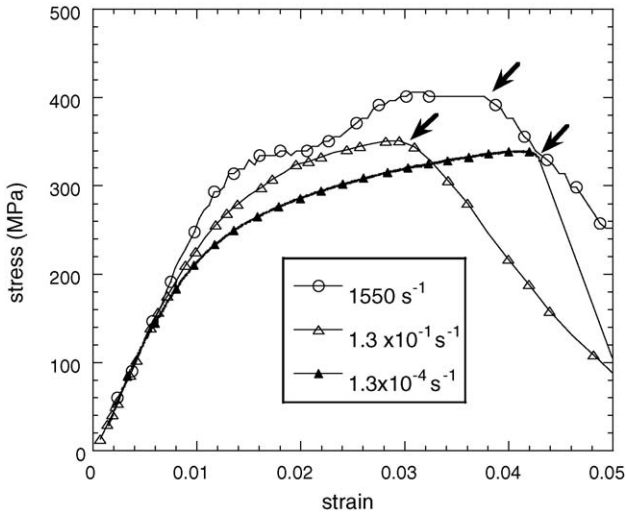
Fig. 3. Typical stress–strains curves of the composite at different strain rates tested in transverse direction (arrows show failure).

corresponding strain are considered to be the failure stress or compressive strength (marked by arrows in Fig. 3) and failure strain respectively. The effect of increasing strain rate is to increase flow stress and failure stress values of the composite as shown in Fig. 4. The flow stress at 2% strain increases from 310 to 350 MPa on the average, when the strain rate increases from quasi-static to high strain rate. Similarly, the compressive strength increases from 350 MPa at quasi-static strain rates to 400 MPa at high strain rates. Increasing the strain rate decreases the failure strain (Fig. 5). The failure strain at $1 \times 10^{-4}\,\mathrm{s}^{-1}$ is about 4%, while it decreases to about 3% when the strain rate is higher than $1 \times 10^{-1}\,\mathrm{s}^{-1}$.

3.2. Longitudinal direction

Testing of unidirectionally reinforced composites in the longitudinal direction is problematic because the deformation and
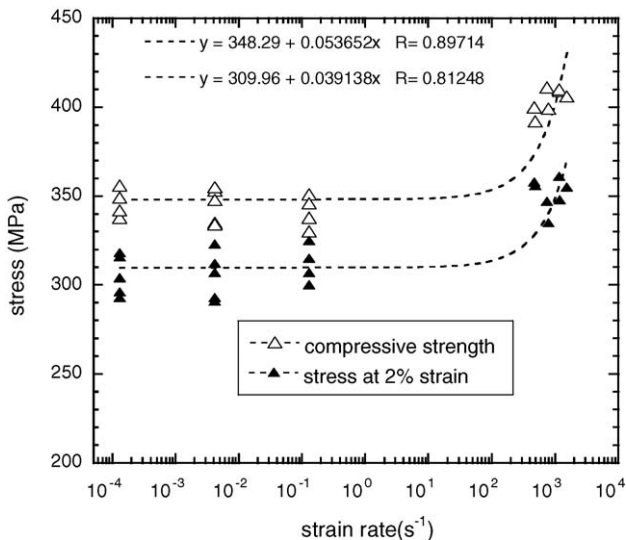

Fig. 4. Variation of compressive strength and flow stress at 2% strain with strain rate in transverse direction.
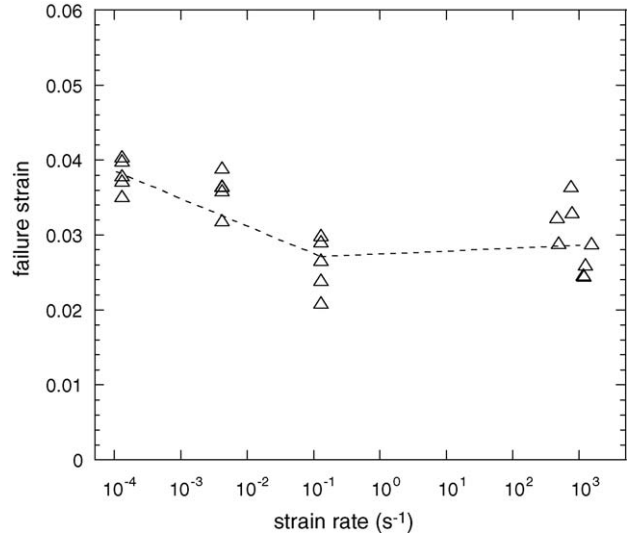

Fig. 5. Variation of failure strain with strain rate in transverse direction.

failure modes are strongly dependent upon the precise loading configuration. Initial tests were conducted using three different configurations: (a) without steel end-caps, (b) with steel end-caps (Fig. 6(a)) and (c) with steel end-caps and dog-bone shaped specimen. The end-caps contained a 0.8 mm deep recess into which the specimen was press fitted to prevent end brooming. Specimens tested without end-caps failed prematurely by axial splitting and brooming occurring at one of the ends of the specimen (Fig. 6(b)). The use of dog bone shaped specimen also resulted in premature failure of the composite (Fig. 6(c)) by splitting near one of the end-caps. The highest maximum stresses were consistently obtained from the cylindrical samples tested with end caps (Fig. 7) and all further testing of the composite was continued with end-caps.

Typical stress–strain curves of the composite in the longitudinal direction at dynamic and quasi-static strain rates are shown in Fig. 8. It can be noted that the stress–strain curve is almost linear until maximum stress (marked with arrow in Fig. 8) with a compression modulus of about 100 GPa. Fig. 9(a) and (b) shows the variation of failure stress and strain with strain rate, respectively. Despite the large variation in failure stress values, the composite showed almost no strain rate dependency in failure stress in the longitudinal direction, although failure stresses are slightly higher on average at the lowest quasi-static rate, $1 \times 10^{-4}\,\mathrm{s}^{-1}$. The failure strain is slightly affected by the strain rate as shown in Fig. 9(b). The failure strain is 2.5% at $10^{-4}\,\mathrm{s}^{-1}$ and decreases to 2% on the average at $10^3\,\mathrm{s}^{-1}$ strain rates.

4. Microscopy

4.1. Transverse direction

The failure mode in this direction at quasi-static and high strain rates was through shear of the matrix, at 45° to the compression loading and fiber axis and is shown in Fig. 10. The failed composite samples tested at quasi-static and dynamic strain rates were sectioned and polished normal to the fiber axis (Fig. 10) so
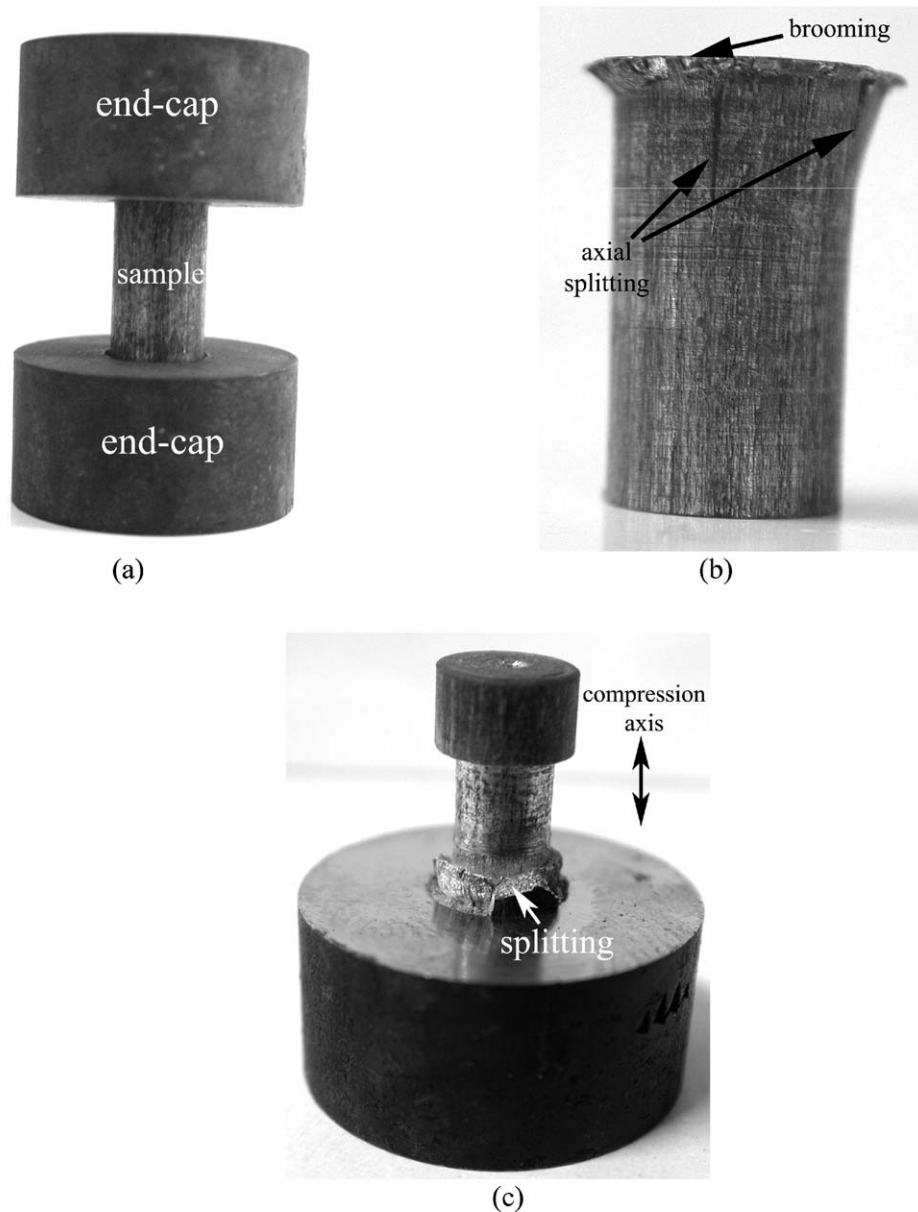
Fig. 6. (a) Compression test specimen with end-caps, (b) failed specimen without end-caps and (c) failed dog-bone shape sample with end-caps.

that features on the fracture surface could be correlated with the underlying microstructure. The fracture surfaces of the failed samples (separated in two pieces) at different strain rates were also analyzed through the mid-sections of the fracture surface as shown by the arrow in Fig. 10.

Fig. 11(a) and (b) shows typical fracture surfaces of the samples tested quasi-statically at low and high magnifications, respectively. The presence of a larger number of fibers on the fracture surface (Fig. 11(a)) and fiber debonding (Fig. 11(b)) confirm a relatively ductile failure mode of the composite through the fiber-matrix interface. Extensive microscopic observation of the fracture surfaces of the samples tested at $750 \, s^{-1}$ revealed a very similar failure mode of the composite at high strain rates except the mating surfaces were slightly smeared in these samples. Fig. 12(a) and (b) shows the highly deformed region comprising twins next to the fracture surface in a quasi-

statically tested sample. The twin intensity was observed to decrease as the distance from the failure region increased and increased in the region of fiber clusters. Twin formation between the fibers, at an intersection with a grain boundary, and multiple twinning and twin intersections with the fiber/matrix interface at quasi-static and dynamic strain rates are shown in Fig. 13(a)–(c). Similar to the quasi-statically tested samples, high strain rate samples $(750 \, s^{-1})$ formed a highly deformed narrow region next to the failure surface (Fig. 14(a)). Cracking of grain boundary precipitates at twin intersections was also seen in these samples (Fig. 14(b)). Detailed microscopic observation of the failure surface revealed wavy slip lines on the surface especially near the debonded fibers in samples tested at quasi-static strain rates (Fig. 15(a)). Although slip lines were also seen in high strain rate tests, cleavage (Fig. 15(b)) was frequently observed as well.
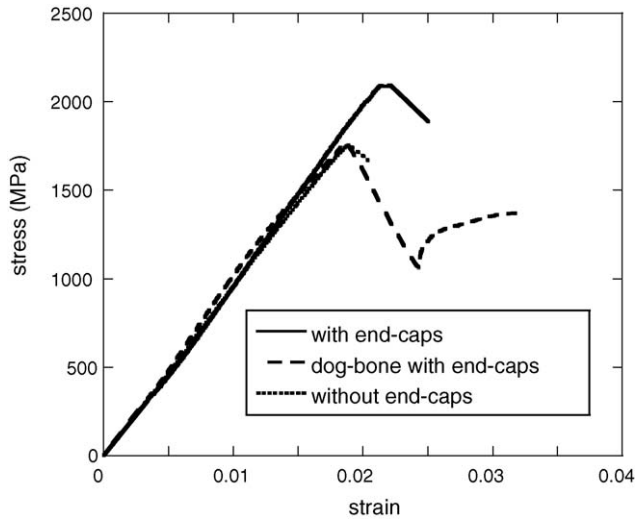
Fig. 7. Typical quasi-static (1.3×10^{-4} s^{-1}) stress–strain curves of composite samples with end-caps, dog-bone shape with end-caps and without end-caps.

4.2. Longitudinal direction

Two types of failure mechanism were observed in this direction, namely, failures resulting from kink formation and from axial splitting. In Fig. 16(a) and (b) typical modes of failure in composite samples tested at 1×10^{-4} and 500 s^{-1} are presented. The sample of Fig. 16(b) was tested at high strain rate and failed by kinking and axial splitting with the splitting occurring after, or in parallel with, kinking. Small areas of the split regions were also observed in quasi-statically tested samples.

Extensive fiber fracture by buckling was observed at kink boundaries and within the kink region (Fig. 17(a)). It should be noted here that a buckled fiber generates a tensile stress in the matrix on one side and a compressive stress at the other side. Tensile stresses tend to form highly deformed regions or voids
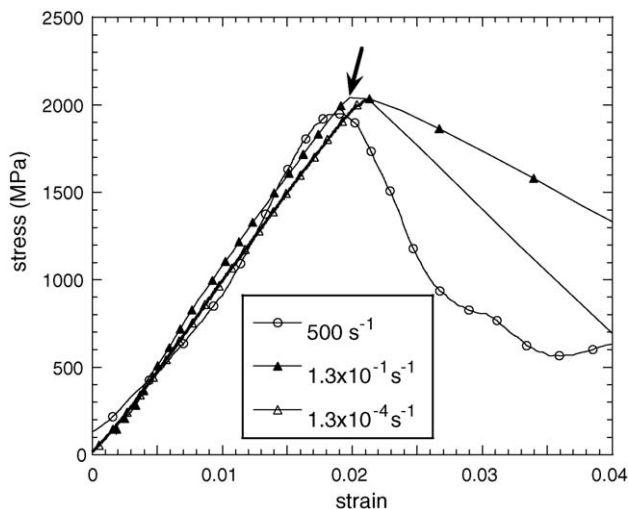

Fig. 8. Stress–strain curves of the composite at different strain rates in the longitudinal direction.
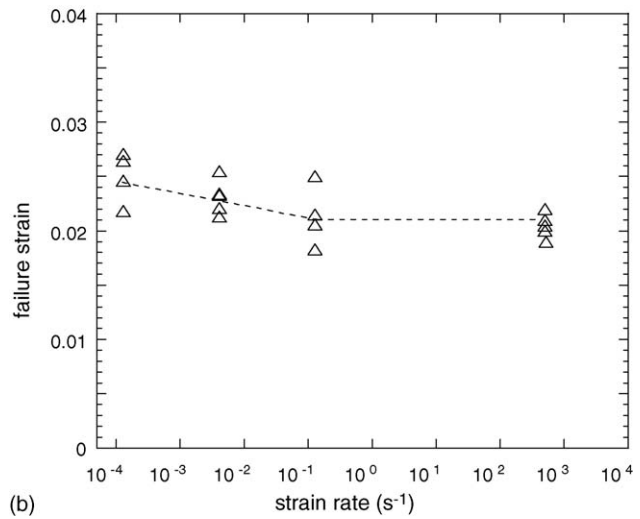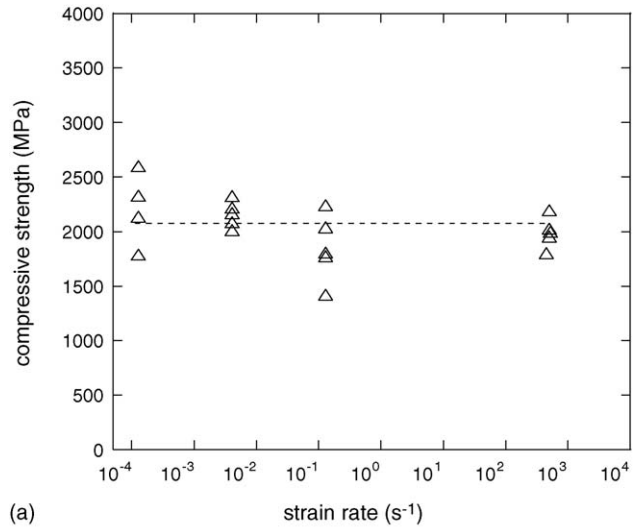

Fig. 9. Variations of (a) compressive strength and (b) failure strain with strain rate in the longitudinal direction.

in the matrix at one side of the fiber while fiber fragments are under compression at the other side This situation is shown in Fig. 17(b) where small fractured but non-separated fiber fragments seen on the top of the fibers correspond to the compression side of the buckled fiber while the fiber-matrix interface failed and opened under tension on the opposite side. The fibers in the kink boundary and in the kink band region fragmented due to the shear strain resulting from micro-buckling.

Shearing of the kink band produced a highly deformed region inside the kink band so that twinning was observed both within the kink band and near the kink band boundaries and at places away from the kink region (Fig. 18(a)). Twinning similar to that in quasi-statically tested samples was also found to occur in the dynamically tested samples. Similar to the transverse direction, in the axial direction the fracture surface (observation made in the samples in which the kinking separated the sample in two pieces) contained wavy slip lines in the matrix (Fig. 18(b)), proving deformation by slip contributes to final deformation in this direction.
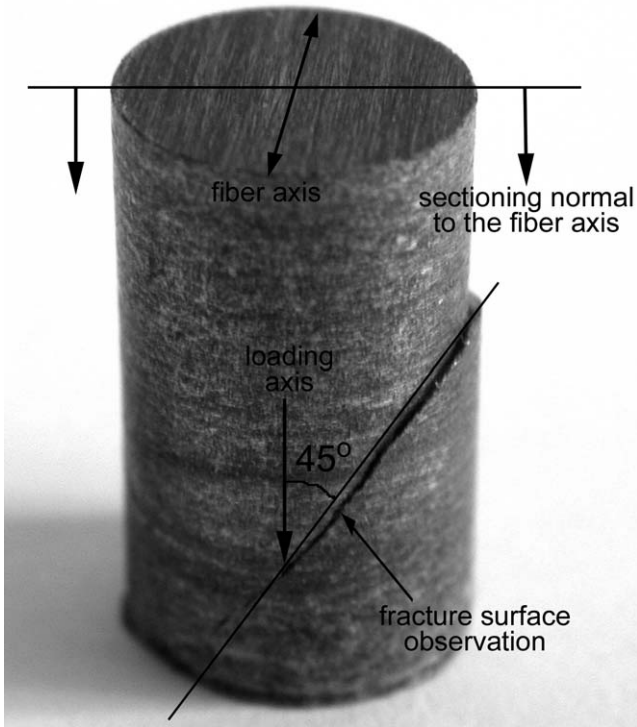
Fig. 10. Image of a failed composite sample tested in transverse direction at 1.3×10^{-4} s^{-1}, showing the failure diagonal to the loading axis and the sections for the microscopic observations.

5. Discussion

The presence of Al in the secondary phases of the composite was most likely due to a reaction between liquid Mg metal with the FP^{TM} fiber during the processing stage, in which Al$_2$O$_3$ was reduced by liquid Mg leading to the release of Al into the melt and concurrent formation of MgO at the melt/oxide interface. The presence of a thin layer of MgO uniformly surrounding the Al$_2$O$_3$ fibers and the formation of Al$_2$MgO$_4$ spinel phase in Mg-alloy composites have been observed in earlier studies [21,22]. Solidification behavior of an Mg–Zn–RE matrix alloy, with a composition similar to the present matrix alloy, was further studied by Wei et al. [23] and it was shown that the α-Mg grains were decorated with a ternary phase of Mg–Zn–RE. Coherent MgZn$_2$-type precipitates parallel to the c-axis of the matrix were also observed in TEM [24].

In order to obtain valid failure stress values during SHPB testing of brittle materials, stress homogenization must occur after about three or four reflections [25]. Therefore, in order to ensure that valid ultimate failure properties are obtained, the limiting strain rate conditions for stress-homogenization must be verified. For brittle materials that show only linear elastic behavior before failure, the nominal strain rate is approximated by the following equation:

$$\dot{\varepsilon} = \frac{\varepsilon_{\mathrm{f}}}{t_{\mathrm{f}}} \tag{5}$$

where ε_{f} and t_{f} are the failure strain and failure time, respectively. Applying the condition of four reflections of the

wave, the limiting strain rate can be determined from the expression:

$$\dot{\varepsilon} = \frac{\varepsilon_{\mathrm{f}} C_{\mathrm{s}}}{4 L_{\mathrm{s}}} \tag{6}$$

where C_{s} is the elastic wave velocity of the sample. Eq. (6) gives a limiting strain rate of ~2000 s^{-1} for the following parameters: $\varepsilon_{\mathrm{f}} \sim 0.02$, $C_{\mathrm{s}} \sim 5000$ m s^{-1} and $L_{\mathrm{s}} \sim 12.8 \times 10^{-3}$ m. The highest average strain rate attained in testing composite in the axial direction was 500 s^{-1}, confirming the validity of compressive strength values measured in this direction.

The mechanical properties of unidirectional composites in the transverse direction are dominated by the matrix properties. However, in terms of damage formation, the presence of fibers normal to the loading direction in compression is significant. Typical damage observations made in MMC's include debonding, fiber fracture, and crushing and matrix fracture on the maximum shear stress plane at ~45° to the compressive loading axis [9,26]. The observations made in this study are similar to those listed above. Therefore, it may be assumed that the rate sensitive flow stress behavior observed in the transverse direction of the composite is due to strain rate sensitive flow stress behavior of the matrix alloy.

Mg has hexagonal closed-packed (hcp) crystal structure with a limited number of slip systems and therefore its ability to deform is limited especially at room temperature. At room temperature, slip occurs predominantly on the basal plane (0 0 0 1) in the $\langle 1\,1\,\bar{2}\,0\rangle$ directions although $\langle c + a \rangle$ slip ($\{1\,1\,\bar{2}\,\bar{2}\}$ $\langle \bar{1}\,\bar{1}\,2\,3\rangle$), which can accommodate compression along the c-axis of the unit cell, was observed in magnesium single crystal when deformed under c-axis compression [27]. Prismatic, $\{1\,0\,\bar{1}\,0\}$, and pyramidal, $\{1\,0\,\bar{1}\,1\}$ and $\{1\,0\,\bar{1}\,2\}$, slip become more important at increasing temperatures [28,29]. In addition to slip on the basal plane, twinning on the $\{1\,0\,\bar{1}\,2\}$ $\langle \bar{1}\,0\,1\,1\rangle$ provides an additional means of deformation. Double twinning, involving $\{1\,0\,\bar{1}\,1\}$ followed by $\{1\,0\,\bar{1}\,2\}$ has also been shown to be important and facilitates compression along the c-axis [29]. The extensive cold rollability of Mg alloys containing certain rare earth elements (e.g. Ce) was further characterized by the presence of deformation bands diagonally inclined to the rolling plane [30]. These bands were suggested to form in the regions of double twinning that allowed preferential alignment of the easy glide planes for slip and concentration of deformation within these bands [30,31].

At room temperature the plastic deformation by slip was demonstrated in Fig. 15(a) by the uneven configuration (different slip planes) of intersecting slip lines due to the activation of basal and non-basal slip systems. The presence of debonded fibers on the fracture surfaces of the tested samples (Figs. 11, 12(a) and 14(a)) further showed that fiber debonding was effective in promoting the development of failure at both the quasi-static and high strain rates. In regions adjacent to the final fracture surface, the strain increased locally due to the maximum shear stresses operating at 45° to the loading axis. The increased local strain was evidenced by a region of severe deformation just next to the fracture and led to the extensive twin formation (twin bands) clearly seen in Figs. 12 and 14.
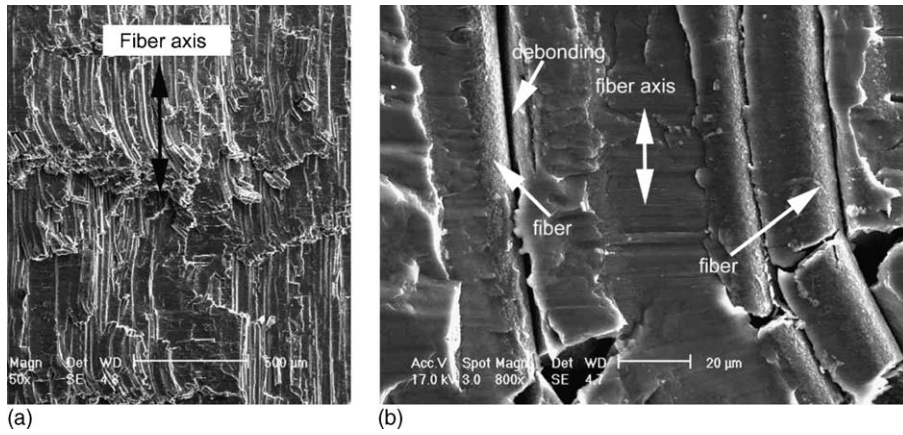
Fig. 11. Fracture surface images of a sample tested at $1.3 \times 10^{-4}\,\text{s}^{-1}$ showing (a) fibers and (b) fiber debonding on the surface.
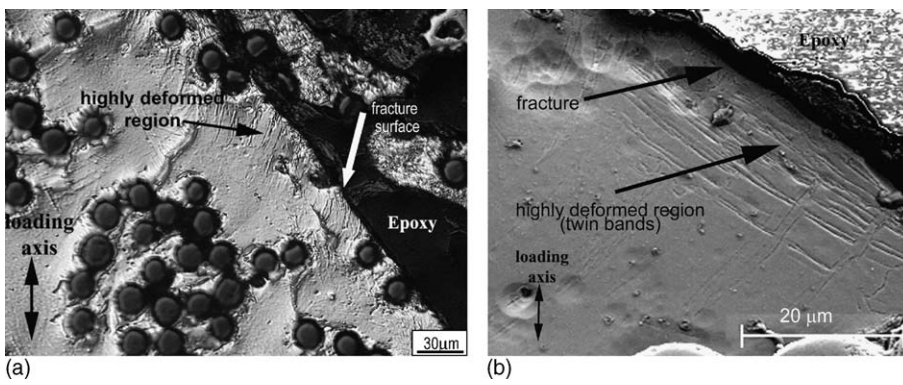

Fig. 12. Polished and highly etched cross-section (normal to the fiber axis) of a failed sample tested at $4.3 \times 10^{-3}\,\text{s}^{-1}$ (failure strain 0.032) showing (a) severe deformation and (b) extensive twin formation next to the failure.
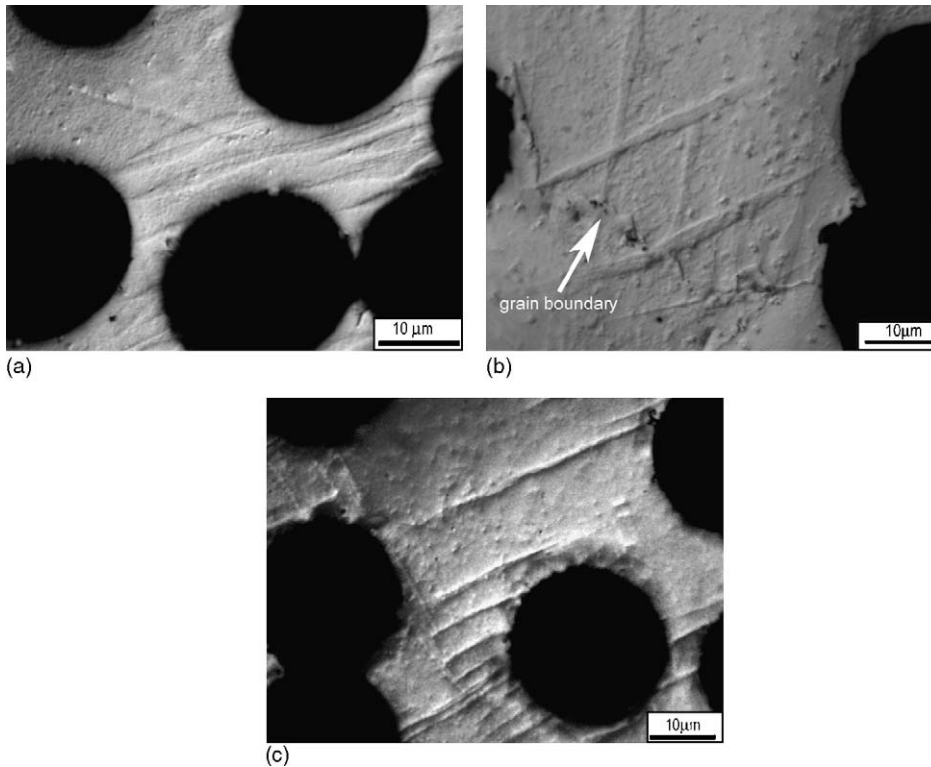

Fig. 13. Optical microscope images of twins in polished and highly etched cross-sections (normal to the fiber axis) of the failed samples tested at (a) $1.3 \times 10^{-4}\,\text{s}^{-1}$ and (b) and (c) $750\,\text{s}^{-1}$.
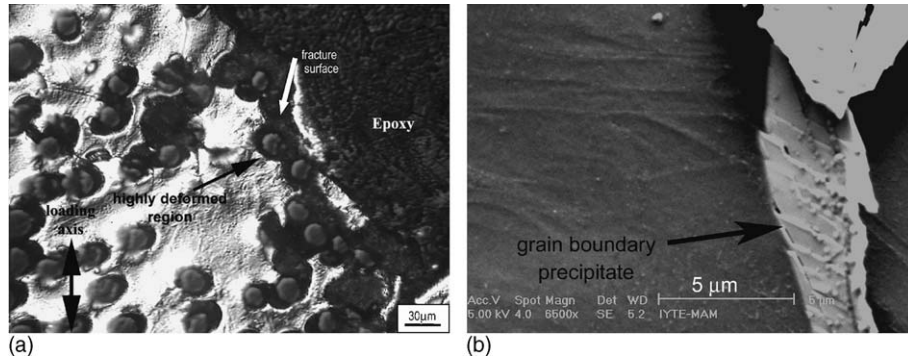
Fig. 14. Polished and highly etched cross-section (normal to the fiber axis) of a failed sample tested at $750\,s^{-1}$ showing (a) severely deformed region and (b) cracked precipitate at twin intersections next to the failure.
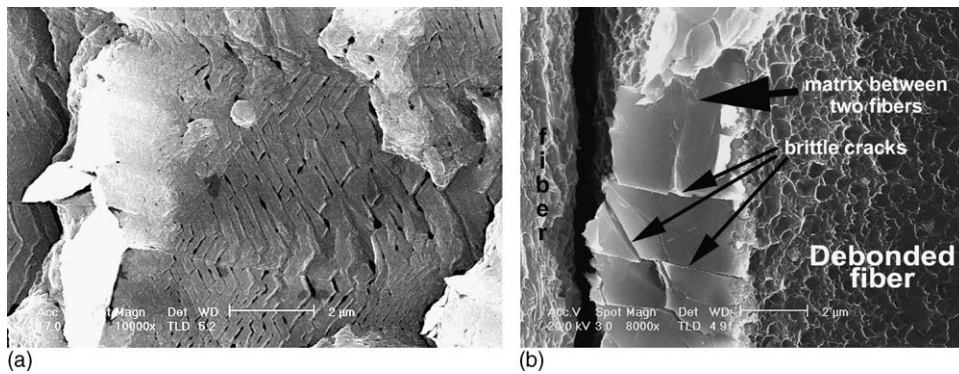

Fig. 15. SEM images of fracture surfaces showing (a) slip lines on the fracture surface near to fiber matrix interface in a sample tested at strain rate $1.3 \times 10^{-4}\,s^{-1}$ and (b) fiber debonding and brittle cracks in the matrix in a sample tested at $750\,s^{-1}$.

Although the polished cross sections of the deformed sample contained many twins, particularly near the failed section of the specimen, the evidence of single and multiple slip on the fracture surfaces indicates that slip is the dominant deformation mechanism. Therefore, it may be concluded that deformation is thermally activated for the tested composite sample in the transverse direction. Similar results have been shown for α-Ti [32], Previous studies on Mg alloys have shown that the flow stress increased with increasing strain rate [12,15,18,33] and the measured strain rate sensitivity of the composite in the transverse direction is due to matrix strain rate sensitivity.

The failure mode in the axial direction is predominantly due to fiber microbuckling parallel to the loading axis, except that axial splitting was also promoted at high strain rates. Therefore, the compressive strengths were essentially governed by the composite shear stress–strain response. For composites following the
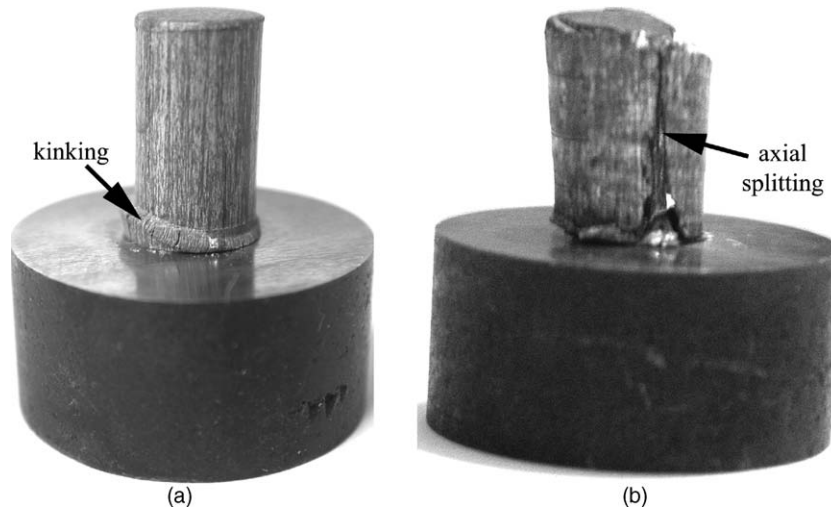

Fig. 16. Failed composite sample tested longitudinally at: (a) $1.3 \times 10^{-4}\,s^{-1}$ and (b) $500\,s^{-1}$.
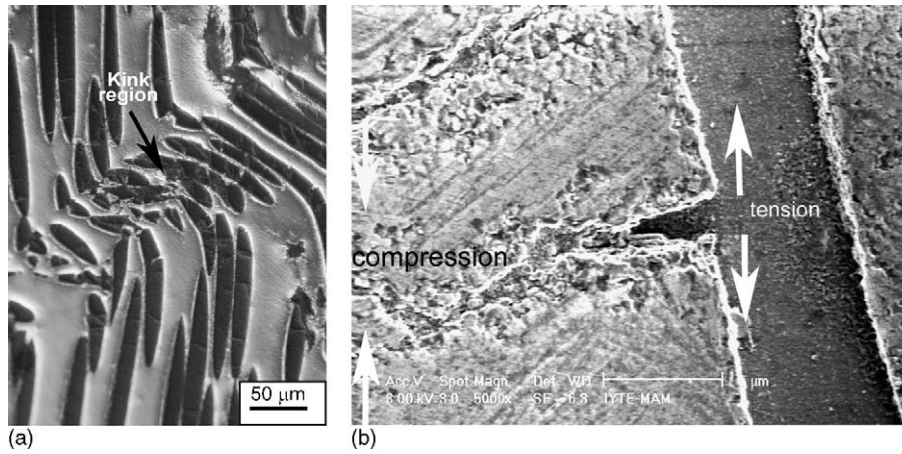
Fig. 17. (a) Kink band progression in a sample deformed at $500\,s^{-1}$ and (b) fiber buckling and formation of tension and compression regions in the matrix in a sample tested at $1.3 \times 10^{-4}\,s^{-1}$.

Ramberg–Osgood shear stress–strain response, the compressive strength is predicted from the relationship [34]:

$$\sigma_c = \frac{G}{1 + n\left(\frac{3}{7}\right)^{1/n}\left(\frac{\phi/\gamma}{n-1}\right)^{n-1/n}} \tag{7}$$

where G is the shear modulus of the composite (G_{12}), n the strain hardening exponent for Ramberg–Osgood power law hardening in shear, γ_y the composite yield strain in the longitudinal shear and ϕ is the average fiber misorientation. The compressive strength was predicted using the above equation. The composite shear modulus was approximated using the relation [35]:

$$G = \left[\frac{f}{G_f} + \frac{1-f}{G_m}\right]^{-1} \tag{8}$$

where G_f and G_m are the fiber and matrix shear modulus and typical values are 130 and 26 GPa, respectively. Fiber misorientations of 0–5° are common for the long fiber composites [11]. The following parameters were used: $G = 25$ GPa, $\phi = 3°$ and $\gamma_y = 0.0055$. The value of n for magnesium alloys in tension varies between 3.6 and 15 [36]. The value of n for 50% FP fiber reinforced 6061-T6 alloy composite was reported 8 [11] and for the comparison the same n value was used in the cal-

culations. The shear yield strain was calculated by dividing the matrix shear strength ($\sim$138 MPa [37]) by the composite shear modulus. Using the above parameters, the composite strength in the axial direction was found to be 2400 MPa, higher than that of average quasi-static fracture strength, 2100 MPa. This shows that a significant portion of the predicted strength ($\sim$90%) is actually developed by the composite. The compressive strength of a FP^{TM} fiber reinforced Al–3% Li composite with the same fiber volume fraction was found to be around 1800 MPa at quasi-static strain rates [10]. The relatively higher compressive strength of the present composite simply arises from the higher shear strength of the matrix. It is noted that calculated values are only approximate and as the fiber misorientation increases the compressive strength value decreases.

The compressive strength of FP^{TM}–Mg composite in the axial direction essentially remains constant as the strain rate increases to $100\,s^{-1}$. A possible reason for the lack of strain rate sensitivity of the composite in the axial direction is that the highest strain rate used in the present study may not be high enough to see strain rate sensitive compressive strength behavior. This is because the strain rate effect often becomes significant only above $\sim$1000 s^{-1} in many materials. Lastly, since the composite is relatively brittle in the axial direction, the large variation of
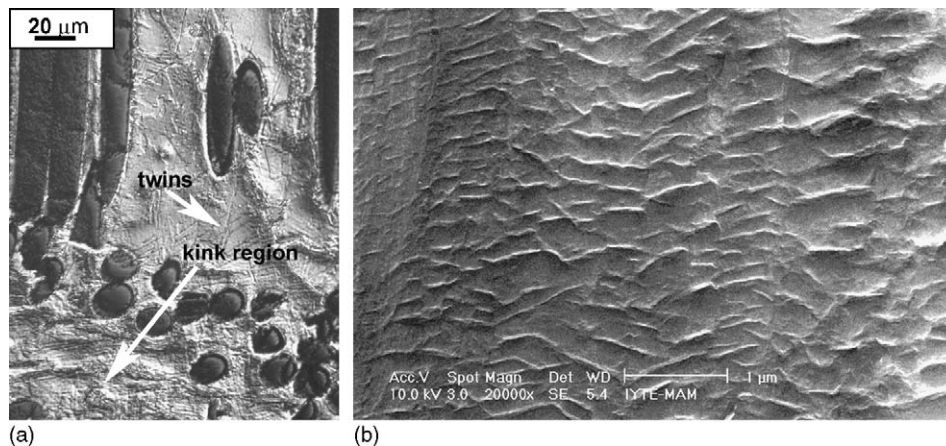

Fig. 18. (a) Highly deformed region in a kink band and (b) slip lines on the fracture surface (sample tested at $1.3 \times 10^{-4}\,s^{-1}$).

the compressive strength, most likely resulting from small misalignments between the fiber and loading axis and tri-axial state of stress imposed by the used end-caps in the tested samples, may mask any rate sensitive behavior.

6. Conclusions

The mechanical response of a continuous FP fiber (35%) Mg composite has been determined in the transverse and longitudinal directions in compression. It was found that, in the transverse direction, the composite exhibited strain rate sensitivity of the flow stress and maximum stress within the studied strain rate range (1.3×10^{-4} to $1500\,\text{s}^{-1}$). However, increasing strain rate decreased the failure strain. Microscopic observations on the failed samples have shown that the composite failed predominantly by shear banding. Although twinning was observed in the deformed cross-sections of the samples at all strain rates, particularly near the shear band region, it was proposed that the main deformation mechanism was slip which was evidenced by the slip lines on the fracture surface. In the longitudinal direction, the composite failed by kink formation at quasi-static strain rates, while kinking and splitting occurred at high strain rates. The maximum stress in the axial direction was, however, found to be strain rate insensitive. The lack of strain rate sensitivity in this direction was attributed to the brittle nature of the composite leading to fluctuation in the compressive strength.

References

[1] Y. Li, K.T. Ramesh, E.S.C. Chin, Acta Metall. Mater. 48 (2000) 1563.
[2] M. Guden, I.W. Hall, Mater. Sci. Eng. A 242 (1998) 141.
[3] H. Zhang, K.T. Ramesh, E.S.C. Chin, Mater. Sci. Eng. A 384 (2004) 26.
[4] G. Bao, Z. Lin, Acta Metall. Mater. 44 (1996) 1011.
[5] A. Marchand, J. Duffy, T.A. Christman, S. Suresh, Eng. Fract. Mech. 30 (1988) 295.
[6] C.-C. Perng, J.-R. Hwang, J.-L. Doong, Mater. Sci. Eng. A 171 (1993) 213.
[7] S.I. Hong, G.T. Gray III, J. Mater. Sci. 29 (1994) 2987.
[8] L.H. Dai, Y.L. Bai, S.-W.R. Lee, Compos. Sci. Tech. 58 (1998) 1667.
[9] C.C. Poteet, I.W. Hall, Mater. Sci. Eng. A 222 (1997) 35.
[10] M. Guden, I.W. Hall, Compos. Struct. 76 (2000) 139.
[11] C.M. Cady, G.T. Gray III, Mater. Sci. Eng. A 298 (2001) 56.
[12] P. Klimanek, A. Pötzsch, Mater. Sci. Eng. A 234 (2002) 145.
[13] T. Mukai, M. Yamanoi, H. Watanabe, K. Ishikawa, K. Higashi, Mater. Trans. 42 (2001) 1177.
[14] H. Watanabe, T. Mukai, M. Mabuchi, K. Higashi, Scr. Mater. 41 (1999) 209.
[15] H. Takuda, S. Kikuchi, T. Tsukada, K. Kubota, N. Hatta, Mater. Mater. Sci. Eng. A 271 (1999) 251.
[16] T. Mukai, M. Yamanoi, K. Higashi, Mater. Trans. 42 (2001) 2652.
[17] K. Ishikawa, H. Watanabe, T. Mukai, Mater. Lett. 59 (2005) 1511.
[18] Y.E.-S. Essa, J.L. Pérez-Castellanos, J. Mater. Proc. Technol. 143/144 (2003) 856.
[19] Y.E.-S. Essa, J. Fernandez-Saez, J.L. Pérez-Castellanos, Compos. B 34 (2003) 551.
[20] High strain rate tension and compression tests ASM Handbook, Mechanical Testing and Evaluation, vol. 8, ASM International, 2000.
[21] W.S. Wolbach, S.R. Bryan, G.L. Shoemaker, T.W. Krucek, R.D. Maier, K.K. Soni, J.M. Chabala, R. Mogilevsky, R. Levi-setti, J. Mater. Sci. 32 (1997) 1953.
[22] J. Kiehn, K.U. Kainer, P. Vostry, I. Stulikova, Phys. Status Solidi 161 (1997) 85;
J. Kiehn, K.U. Kainer, P. Vostry, I. Stulikova, Phys. Status Solidi 161 (1997) 85.
[23] L.Y. Wei, G.L. Dunlop, H. Westengen, J. Mater. Sci. 32 (1997) 3335.
[24] Z. Trojanová, V. Gartnerová, P. lukac, Z. Drozd, J. Alloys Compd. 378 (2004) 19.
[25] G. Ravichandran, G. Subhash, J. Am. Ceram. Soc. 77 (1994) 263.
[26] B.J. Weng, S.T. Chang, S.E. Hsu, Mater. Sci. Eng. A 156 (1992) 143.
[27] T. Obara, H. Yoshinga, Morosumi, Acta Metall. 21 (1973) 845.
[28] C.S. Roberts, Magnesium and Its Alloys, JohnWiley & Sons Inc., New York, 1960.
[29] G.V. Raynor, The Physical Metallurgy of Magnesium and its Alloys, Pergamon Press, New York, 1959.
[30] S.L. Couling, J.F. Pashak, L. Sturkey, Trans. ASM 51 (1959) 94.
[31] M.R. Barnet, M.D. Nave, C.J. Bettles, Mater. Sci. Eng. A 386 (2004) 205.
[32] D.R. Chichili, K.T. Ramesh, K.J. Hemker, Acta Mater. 46 (1998) 1025.
[33] K. Yu, W. Li, J. Zhao, Z. Ma, R. Wang, Scr. Mater. 48 (2003) 1319.
[34] B. Budiansky, N.A. Fleck, J. Mech. Phys. Solids 41 (1993) 183.
[35] T.W. Clyne, P.J. Winters, An Introduction to Metal Matrix Composites, Cambridge University Press, Cambridge, 1993.
[36] Military Handbook: Metallic Materials and Elements for Aerospace Vehicle Structures, MIL_HDBK-5H, Department of Defense, 1998.
[37] Magnesium Elektron, Elektron RZ5 data sheet.